Published by

British Journal of Contemporary Research

BEXFORD PUBLISHING

Groundwater Hydrogeochemistry, Uranium Mobility and Human Health Risk in the Mikir Hills, Assam, India: An Integrated Multivariate, Machine-Learning and Risk-Assessment Framework

Original Research Article | Volume 1 | Issue 6 | 2026 | Article Number: 015

Accepted: 16 October 2026 | Published: 10 November 2026 | ISSN: 2979-8582 (Online)

Crossref : **https://doi.org/10.67693/BJCR-6UTHFG7U**

Ashokaditya P. Dhurandhar

Orion Geohytech India, G-10 Brahmaputra Apartment, Aakar Nagar, Katol Road, Nagpur, India

APD 0000-0002-9948-1937

Correspondence: Ashokaditya P. Dhurandhar, apdhurandhar@gmail.com

Abstract

Groundwater in the Mikir Hills of Assam, India, occurs within a complexly layered lithostratigraphic framework spanning Archaean basement gneisses to Quaternary alluvium. To characterise the hydrogeochemical controls on major ions, trace metals, and uranium (U) behaviour, a dataset of 143 groundwater samples across 16 core parameters (U, Na, K, Ca, Mg, Cl, SO_4^{2-}, HCO_3^-, pH, electrical conductivity, TDS, Cu, Pb, Zn, Ni, and Fe) was evaluated using an integrated multivariate, geochemical, and machine-learning framework. Hydrochemical facies analysis demonstrates that groundwaters are predominantly of Ca–Mg–HCO_3^- (52%) and mixed Ca–Na–HCO_3^- (30%) types, with Gibbs formulations confirming rock–weathering dominance alongside negative chloro–alkaline indices denoting reverse ion exchange. Speciation modeling indicates widespread supersaturation with respect to calcite (SI=+0.42) and dolomite (SI=+0.77), confirming that carbonate buffering establishes circumneutral–to–alkaline conditions. Nonparametric correlation and principal component analysis (PCA; four components explaining 67.2% of total variance) show that U is decoupled from bulk mineralisation (loading −0.04 on PC1) and instead loads on PC3 (0.64) and PC4 (0.35) alongside Cu, Fe, and Zn. Random Forest (RF) regression reveals negative cross–validated performance (R^2=−0.077), whereas RF classification effectively discriminates upper–quartile U concentrations (>0.50 µg/L) with a ROC–AUC of 0.794. The Entropy–Weighted Water Quality Index (EWQI) identifies 38% of samples within poor–to–very–poor categories, driven predominantly by Fe

© 2026 The Authors. Published by Bexford Publishing Ltd

and localized trace elements. Chemical health-risk assessment establishes non-carcinogenic hazard quotients (HQ) exceeding 1.0 in 19% of adult and 31% of child cohorts, with cumulative hazard indices (HI>1.0) reaching 47% and 58%, respectively. These findings demonstrate that U migration is governed by redox-mediated Fe–Mn cycling, carbonate ligand complexation, and structural fracture conduits rather than bulk salinity. Identification of overlapping anomalies in high-strain corridors and fault zones—specifically at the Akashiganga–Udganga Convergence—host a significant alignment of peak gaseous Radon (>1100 counts/50 s) alongside Aqueous Radium (Ra) and Aqueous Uranium (U) anomalies, designating this convergence zone as the prime vector target for concealed mineralization.

Keywords: Groundwater Hydrogeochemistry, Uranium Mobility, Hydrochemical Facies, Mineral Saturation Index, Entropy-Weighted Water Quality Index, Human Health Risk Assessment, Random Forest Classification, Mikir Hills

1. Introduction

Groundwater quality within crystalline massifs and surrounding sedimentary basins is controlled by the interplay of bedrock lithology, structural architecture, rock–water reactions, and localized anthropogenic additions (Güler et al., 2002; Helena et al., 2000). In uraniferous provinces, uranium mobility and associated trace metal dynamics (such as Fe, Cu, Zn, Ni, and Pb) are fundamentally governed by ambient oxidation-reduction potential, solution pH, aqueous speciation, complexation by dissolved inorganic carbon, and surface sorption–desorption phenomena (Adimalla & Wu, 2020; Swift Bird et al., 2020; Zhu et al., 2022). Consequently, localized groundwater uranium anomalies cannot be evaluated through isolated bivariate relationships; they emerge from multidimensional geochemical subsystems operating across variable structural flow regimes (Khurelbaatar et al., 2022).

Multivariate statistical techniques—including principal component analysis (PCA), Spearman rank correlation matrices, and Ward-linkage agglomerative hierarchical clustering (AHC)—are standard tools for deconvolving complex hydrogeochemical signatures into interpretable geochemical processes (Güler et al., 2002; Helena et al., 2000; Patel et al., 2023; Wu & Sun, 2016). More recently, non-parametric machine-learning algorithms, notably Random Forest (RF) architectures, have supplemented ordination techniques by identifying non-linear threshold controls and ranking predictor importance (Breiman, 2001; Song et al., 2025). Rigorous computational hydrogeology requires assessing predictive models via out-of-sample cross-validation, where negative skill scores on continuous targets provide critical physical insights regarding system non-linearity and data limitations (Khurelbaatar et al., 2022).

To transform statistical descriptions into actionable hydrogeological frameworks, three supplementary analytical domains are essential:

1. **Hydrochemical Facies and Geochemical Evolution:** Piper trilinear diagrams and Gibbs bivariate plots classify water types, map evolution pathways, and distinguish atmospheric recharge, rock weathering, and evaporative concentration mechanisms (Gibbs, 1970; Piper, 1944).
2. **Entropy-Weighted Water Quality Index (EWQI):** Integrating multi-element compositions into an objective composite metric eliminates expert bias by computing information-entropy weights

© 2026 The Authors. Published by Bexford Publishing Ltd

directly from parameter dispersion relative to international standards (Islam et al., 2017; Li et al., 2010).

3. **Probabilistic Human Health Risk Assessment (HHRA):** Implementing the USEPA chronic intake framework evaluates the chemical nephrotoxicity and trace metal hazard indices for adult and pediatric populations via ingestion and dermal pathways (USEPA, 1989; WHO, 2022).

Despite expanding research on groundwater uranium occurrences across peninsular and northwestern India (Nepolian et al., 2022; Pandit et al., 2022), systematic hydrochemical appraisals integrating mineral saturation modelling, machine learning, and health risk frameworks remain scarce for the complex Precambrian cratonic fragments of northeastern India. The Mikir Hills massif in Assam exposes an ancient crystalline core with documented radioactive mineral occurrences, structural fracture networks, and ferruginous strata—favorable settings for mobilization (Nepolian et al., 2022).

This investigation evaluates 143 representative groundwater samples from the Mikir Hills to:

- Characterise hydrogeochemical variations and identify primary solute-acquisition mechanisms using trilinear projections, ionic ratios, and chloro-alkaline metrics.
- Resolve underlying geochemical processes via PCA and Ward-linkage clustering.
- Model mineral saturation states (SI) with PHREEQC to evaluate carbonate, sulfate, and oxyhydroxide equilibria.
- Determine drinking-water safety using the objective EWQI formulation.
- Quantify exposure risks (HQ and HI) across adult and pediatric cohorts using the USEPA model.
- Test predictive capabilities of cross-validated RF regression versus classification architectures for uranium occurrence.
- Identify the subsurface targets for uranium occurrence.

2. Geological and Hydrogeological Setting

The Mikir Hills (Karbi Anglong plateau) form an uplifted, dissected Precambrian cratonic block separated from the Shillong Plateau to the southwest and surrounded by the Neogene–Quaternary Brahmaputra alluvial plains. The lithostratigraphic framework spans from Archaean granitic basements through Proterozoic metasediments, Mesozoic igneous complexes, and Tertiary sandstones to unconsolidated Quaternary sediments (Table 1and Figure 1).

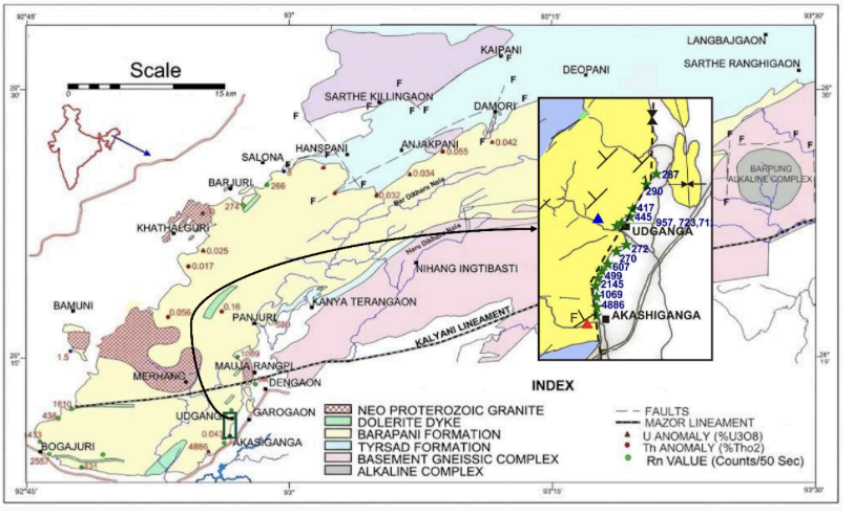


Figure1. Geological map of the Mikir Hills showing uranium, thorium, and radon values inset blown up part of Akashiganga-Udganga area with water radon and radium anomalies

© 2026 The Authors. Published by Bexford Publishing Ltd

Table 1: Lithostratigraphic Framework and Hydrogeological Significance of the Mikir Hills, Assam

Stratigraphic Era	Group / Formation	Dominant Lithology	Structural & Hydrogeological Role
Quaternary	Alluvium / Valley Fill	Unconsolidated gravel, sand, silt, and clay	Porous, unconfined shallow aquifers; active alluvial recharge zones.
Tertiary	Jaintia / Barail Groups	Sandstones, carbonaceous shales, and thin coal seams	Intergranular and fracture-dominated porosity; variable permeability.
Cretaceous–Jurassic	Alkaline / Ultrabasic Intrusives	Carbonatites, lamprophyres, and dolerite dykes	Deep-seated fracture systems; localized lineament-bound pathways.
Middle–Late Proterozoic	Shillong Group (Barapani Formation)	Quartzites, magnetite-bearing sandstones, conglomerates	Secondary fracture permeability; localized ferruginous mineralization horizons.
Early Proterozoic	Tyrsad Formation	Volcaniclastic schists, phyllites, and ferruginous quartzites	Strongly sheared, deformed fracture network; conduit for localized fluid flow.
Archaean	Basement Complex	Granitic gneisses, migmatites, and amphibolites (~2670 Ma)	Crystalline basement; groundwater restricted to weathered regolith and jointed bedrock.

Groundwater circulation occurs within two principal regimes: secondary weathered zones (saprolite/regolith) and deep structural joints and shear zones traversing crystalline gneisses, alongside primary intergranular porosity within Shillong Group sandstones and Quaternary valley fills. Major tectonic lineaments, faults, and shear zones create preferential pathways for meteoric recharge and structurally channel uraniferous fluids in the presence of magnetite-bearing strata.

3. Materials and Methods

3.1. Sampling and Analytical Techniques

Groundwater samples (n=143) were collected during 2003–2004 from boreholes fitted with hand pumps, open dug wells, and natural fractures. Field parameters (pH, electrical conductivity [EC], and temperature) were measured immediately at the wellhead using multi-parameter portable meters calibrated with standard buffer solutions (Sundaram et al., 2009). Samples collected for major ions and trace metals were filtered through 0.45 μm cellulose membranes; trace-element aliquots were acidified to pH<2 using ultrapure sub-boiling HNO_3 (APHA, 2023).

Major anions (Cl^-, SO_4^{2-}, HCO_3^-) were quantified via standard titrimetry and ion chromatography. Cations (Na^+, K^+, Ca^{2+}, Mg^{2+}) were measured by flame atomic absorption spectrometry (FAAS), and total

© 2026 The Authors. Published by Bexford Publishing Ltd

dissolved solids (TDS) were determined gravimetrically at 180°C. Trace metals (Fe, Cu, Pb, Zn, Ni) and uranium (U) were measured using inductively coupled plasma mass spectrometry (ICP-MS) and optical emission spectrometry (ICP-OES). Analytical charge-balance errors (CBE) were evaluated using meq/L units:

$$CBE = \frac{\sum z \cdot m_{cat} + \sum z \cdot m_{an}}{\sum z \cdot m_{cat} - \sum z \cdot m_{an}} \times 100 \quad (1)$$

Samples adhering to $|CBE| \leq 10\%$ were retained for primary analysis (Figure 2).

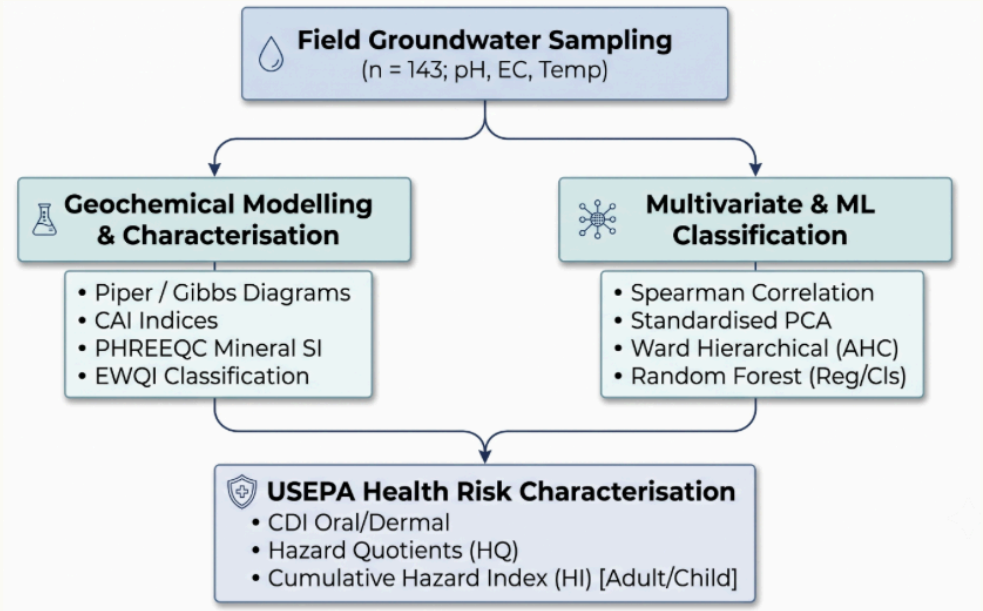


Figure 2. Methodological workflow showing geochemical modeling, multivariate ordination, machine learning, and health risk assessment.

3.2. Geochemical Indices and Thermodynamic Speciation

Hydrochemical facies were classified via Piper trilinear diagrams (Piper, 1944). Dominant solute-acquisition mechanisms (precipitation, rock weathering, evaporation) were determined using Gibbs formulations:

$$\text{Gibbs Cation Ratio} = \frac{Na^+}{Na^+ + Ca^{2+}} \quad (2)$$

$$\text{Gibbs Anion Ratio} = \frac{Cl^-}{Cl^- + HCO_3^-} \quad (3)$$

Cation exchange dynamics were evaluated using Chloro-Alkaline Indices (Schoeller, 1965), where ion concentrations are expressed in meq/L:

$$CAI - 1 = \frac{Cl^- - (Na^+ + K^+)}{Cl^-} \quad (4)$$

$$CAI - 2 = \frac{Cl^- - (Na^+ + K^+)}{SO_4^{2-} + HCO_3^- + CO_3^{2-} + NO_3^-} \quad (5)$$

Mineral saturation indices (SI=log[IAP/Ksp]) for calcite, dolomite, gypsum, fluorite, and quartz were computed via PHREEQC v3 using the phreeqc.dat thermodynamic database (Parkhurst & Appelo, 2013). Samples falling within

© 2026 The Authors. Published by Bexford Publishing Ltd

$-0.1 \leq SI \leq +0.1$ represent thermodynamic equilibrium; values $>+0.1$ indicate supersaturation (precipitation tendency), and values <-0.1 indicate undersaturation (dissolution tendency) (Langmuir, 1997).

3.3. Entropy-Weighted Water Quality Index (EWQI)

The EWQI was computed across 15 hydrochemical parameters (pH, TDS, Total Hardness, Na^+, K^+, Ca^{2+}, Mg^{2+}, Cl^-, SO_4^{2-}, HCO_3^-, Fe, U, Pb, Zn, and Ni) using Shannon entropy to eliminate subjective weight assignments (Islam et al., 2017; Li et al., 2010):

1. **Matrix normalization:** For measured concentration *Cij* and guideline standard *Sj* (WHO, 2022):$qij=SjCij$
2. **Entropy computation:** Parameter probability $pij=qij/\sum i=1mqij$, leading to information entropy ej:$ej=-\ln m1i=1\sum mpij\ln(pij)$
3. **Weight evaluation:** The information utility value $dj=1-ej$ defines the relative entropy weight wj:$wj=\sum j=1ndjdj$
4. **Aggregation:**EWQI=$j=1\sum n(wj\times SjCij\times 100)$Water suitability is categorized as: Excellent (<25), Good (25–50), Medium (50–100), Poor (100–150), and Very Poor (>150).

3.4. USEPA Human Health Risk Assessment Model

Non-carcinogenic chemical toxicity was quantified for adults (70 kg body weight, 2.0 L/day intake) and children (15 kg body weight, 1.0 L/day intake) over an exposure frequency of 365 days/year (USEPA, 1989, 2004):

$$CDIoral=BW\times ATC\times IR\times EF\times ED \quad (6)$$

$$CDIdermal=BW\times ATC\times SA\times Kp\times ET\times EF\times ED\times CF \quad (7)$$

The Hazard Quotient (HQ) was calculated against the chronic oral reference dose (RfD for U is $0.6\times10-3$ mg/kg/day; USEPA, 2010):

$$HQ=RfDCDI \quad (8)$$

$$\text{Hazard Index (HI)}=k=1\sum pHQk \quad (9)$$

HQ or HI>1.0 indicates potential adverse non-carcinogenic health effects.

3.4. Coupled Radon (^{222}Rn) and Radium (^{226}Ra) Surveys: Decoupled Gaseous and Solute Dynamics

The distinct physical states and geochemical behaviors, dissolved radium isotopes and inert gaseous radon cannot be evaluated interchangeably and require separate, parallel investigative protocols:

- **Radon (^{222}Rn) Gaseous Phase Degassing and Fracture Transport:** As an unreactive noble gas with a short half-life ($t1/2=3.82$ days), dissolved 222Rn acts primarily as an *in situ* physical tracer of active structural discontinuities, localized degassing, and rapid groundwater transit rather than conservative solute mass transport. Field screening necessitates closed-loop, on-site alpha scintillation or pulsed ionization chamber detection directly at the wellhead to prevent atmospheric evasion and quantify lineament-guided flow pathways.

- **Radium (^{226}Ra) Aqueous Solvation and Ion-Exchange Controls:** Unlike its gaseous daughter, parent 226Ra ($t1/2\approx1,600$ years) behaves as an alkaline earth divalent cation (Ra2+). Its aqueous mobility is strongly governed by competitive cation exchange on clay substrates, co-precipitation in secondary barite/carbonate minerals, and salinity-driven desorption. Quantification requires dedicated radiochemical separation and gamma or alpha spectrometry to evaluate direct ingestion-dose radiological hazards independently from volatile inhalation pathways.

© 2026 The Authors. Published by Bexford Publishing Ltd

3.4.1. Radon Emanometric and Radiometric Dispersion

Radon (^{222}Rn) emanometry across the Barhola–Hanspani and Akashiganga – Udganga – Dongphlang – Dirabasti – Hayajuri sectors of the Mikir Hills reveals a distinct, structurally guided radiogenic dispersal pattern. Regionally, spot radon counts rise systematically from baseline values along the Hanspani Shear Zone (e.g., 266 counts/50 s at Barjuri, 274 near Khathalguri, and 580 at Panjuri) to intense radiometric anomalies southward along the Kalyani Lineament and its associated splay faults (Figure 1). These elevated values include 1,069 counts/50 s at Mauja Rangpi, 438–2,557 counts/50 s across the Bogajuri corridor, and a survey maximum of 4,886 counts/50 s at Akashiganga. Because these radiometric highs trace mapped fault planes rather than lithostratigraphic contacts, structural discontinuities clearly control gaseous advective transport.

Detailed sampling across the Akashiganga–Dongphlang–Dirabasti–Hayajuri sector highlights a dense cluster of anomalous spring radon values (ranging from 272 to 4,886 counts/50 s) concentrated specifically within the Udganga–Akashiganga sector. Crucially, this gas-phase anomaly occurs in direct spatial coincidence with localized aqueous radium and uranium anomalies. Because radon operates as a short-lived, volatile gaseous phase while radium and uranium migrate as dissolved ionic solutes, their strict spatial convergence rules out surficial dispersion and points to a focused, fault-channeled radiogenic source at depth.

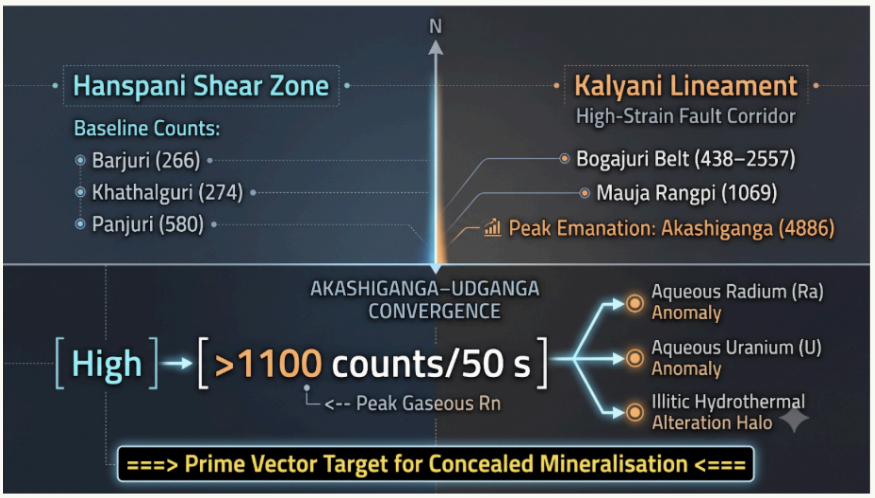


Figure 3. Regional structural trends and spatial convergence of gaseous radon emanation with aqueous radium and uranium anomalies.

Gridded contour mapping illustrates this geometry through a closed anomaly exceeding 900–1,100 counts/50 s centered over Akashiganga–Udganga, which decays concentrically through intermediate intervals (550–850 and 150–500 counts/50 s) down to regional background levels (<100 counts/50 s). A secondary linear anomaly (300–400 counts/50 s) occurs northeast near Bogajuri and Barjuri, aligning with adjacent fault-shear segments (Figure 3,4). The mutual alignment of the gaseous radon high, aqueous radium/uranium anomalies, and documented illitic alteration halos confirms this fault corridor as the primary exploration vector for concealed uranium mineralization (Table 2).

Table 2: Representative Radon Activity and Multi-Nuclide Juxtaposition Across Structural Sectors

© 2026 The Authors. Published by Bexford Publishing Ltd

Sector / Locality	Structural Association	Rn Activity (counts/50 s)	Co-occurring Radiometric Phase	Geochemical / Exploration Role
Barjuri	Hanspani Shear Zone	266	Baseline ambient	Regional background threshold for crystalline basement.
Khathalguri	Hanspani Shear Zone	274	Baseline ambient	Low gaseous permeability along intact shear fabric.
Panjuri	Hanspani Shear Zone	580	Minor localized gas flux	Minor structural relaxation along shear boundary.
Bogajuri Belt	Kalyani Lineament Splays	438–2,557	Elevated emanometry	Dilatant fracture-guided upward advection of gas.
Mauja Rangpi	Kalyani Fault System	1,069	Elevated emanometry	High-permeability fracture conduit.
Udganga–Akashiganga	Fault Junction / Fracture Zone	**272–4,886** (Peak: 4,886)	**Juxtaposed 222Rn gas, aqueous 226Ra, and dissolved U**	Primary exploration target; confirms localized bedrock leaching and active ascent ahead of exploratory drilling.

© 2026 The Authors. Published by Bexford Publishing Ltd

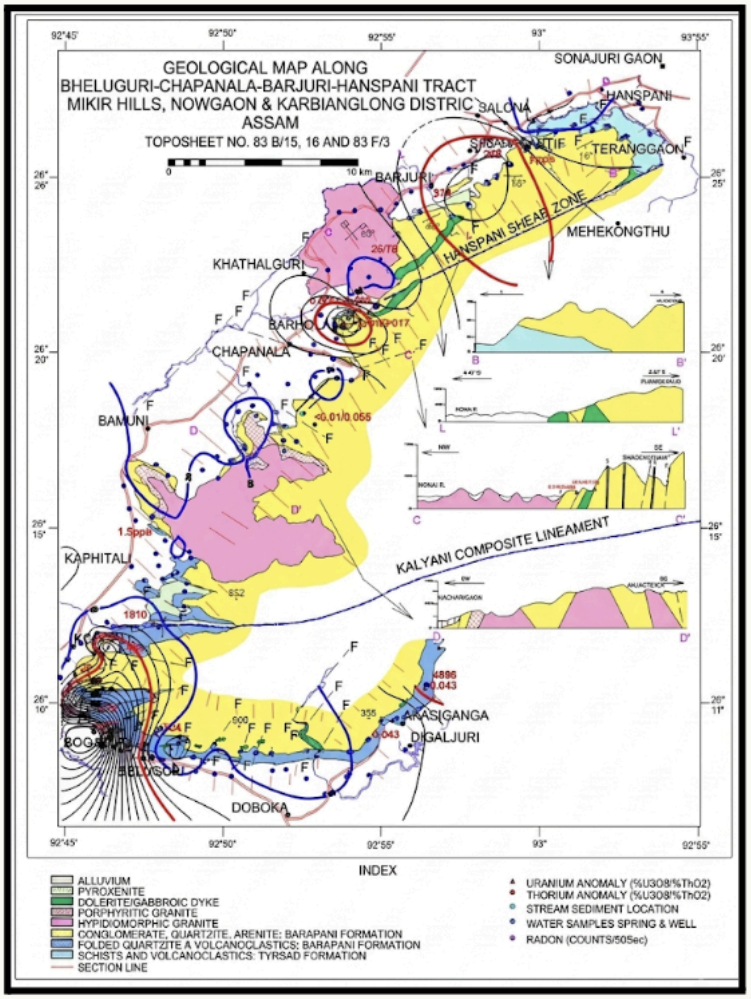


Figure 4. Geological sketch map showing hydrogeochemical sampling stations and superimposed 222Rn emanometry contours across the Akashiganga–Bogajuri fault corridor.

3.5. Multivariate Ordination and Machine Learning

Given positive skewness in U and trace metal concentrations, variables were transformed to log10(x) (except pH) and standardized to zero mean and unit variance. PCA was performed with component retention based on eigenvalues >1.0 and scree plot inspection. Agglomerative Hierarchical Clustering (AHC) used Ward's minimum-variance linkage and squared Euclidean distances, with cluster separation validated using silhouette scores.

Random Forest models were implemented using 5-fold cross-validation. Continuous prediction was assessed using $R2$, RMSE, and MAE. Upper-quartile uranium discrimination (U>0.50 μg/L) was evaluated via ROC-AUC, Precision, Recall, and out-of-fold permutation feature importance (Breiman, 2001; Khurelbaatar et al., 2022).

4. Results

4.1. Hydrochemical Composition and Baseline Statistics

Groundwater in the Mikir Hills displays wide chemical variations (Table 3). Total dissolved solids range from 24.0 to 1,280 mg/L (mean 184.2 mg/L), indicating variable degrees of rock weathering. Uranium concentrations span from 0.25 to 6.00 μg/L (mean 0.63 μg/L, median 0.50 μg/L). While all samples remain below the absolute WHO (2022) drinking water threshold of 30 μg/L, 25% equal or exceed the

© 2026 The Authors. Published by Bexford Publishing Ltd

upper-quartile threshold of 0.50 μg/L. Dissolved iron ranges from 0.05 to 12,952 μg/L (mean 477.18 μg/L), frequently exceeding the WHO aesthetic guideline of 300 μg/L.

Table 3: Descriptive Statistics of Hydrogeochemical Parameters (*n*=143)

Parameter	Unit	Minimum	Median	Mean	Maximum	Std. Dev.	Skewness	Kurtosis
pH	—	5.80	6.70	6.69	8.40	0.44	0.28	0.94
EC	μS/cm	36.0	240.0	283.4	1960.0	242.1	2.81	11.40
TDS	mg/L	24.0	156.0	184.2	1280.0	157.4	2.80	11.35
Ca2+	mg/L	3.20	24.00	30.12	192.00	24.81	2.65	10.32
Mg2+	mg/L	1.10	8.50	12.18	84.00	11.23	2.74	10.88
Na+	mg/L	1.80	12.40	18.74	148.00	18.90	3.12	13.50
K+	mg/L	0.40	2.10	3.42	42.00	4.88	4.35	24.10
HCO3−	mg/L	18.0	110.0	132.8	680.0	98.4	2.21	6.80
Cl−	mg/L	2.40	14.20	22.45	210.00	25.60	3.48	16.20
SO42−	mg/L	0.80	8.20	14.65	164.00	18.72	3.90	19.80
U	μg/L	0.25	0.50	0.63	6.00	0.68	4.73	28.70
Fe	μg/L	0.05	142.00	477.18	12952.00	1340.20	6.84	56.40
Cu	μg/L	0.10	3.40	7.82	84.00	12.15	3.44	14.60
Pb	μg/L	0.01	0.80	2.15	34.00	4.10	4.52	25.30
Zn	μg/L	1.20	18.50	44.20	480.00	76.50	3.65	15.90
Ni	μg/L	0.10	1.20	2.80	48.00	5.20	5.12	33.10

4.2. Hydrochemical Facies and Rock–Water Interaction Mechanisms

Piper trilinear diagrams resolve three principal hydrochemical water types (Table 4, Figure 5):

© 2026 The Authors. Published by Bexford Publishing Ltd

1. **Ca–Mg–HCO_3^- (52%):** Dominates shallow weathered regolith, reflecting primary silicate hydrolysis and minor carbonate dissolution.
2. **Mixed Ca–Na–HCO_3^- (30%):** Represents intermediate flow systems undergoing moderate cation exchange.
3. **Na–K–Cl / Na–SO_4^{2-} (18%):** Reflects evolved groundwater with prolonged contact times along deep fractures or localized mineral dissolution.

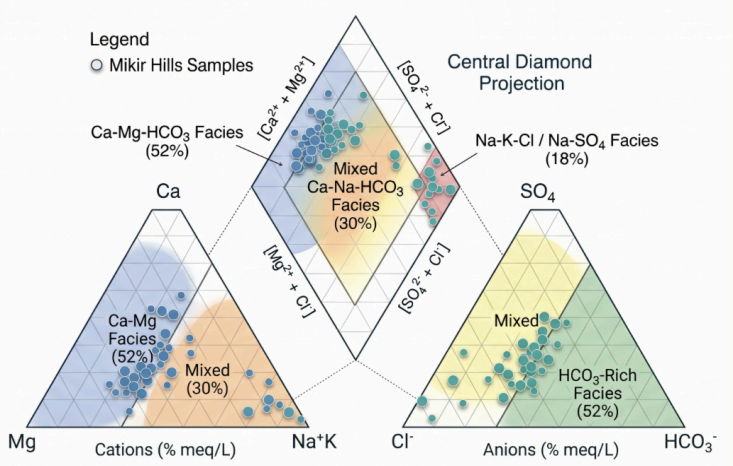


Figure 5. Conceptual Piper trilinear diagram showing the distribution of hydrochemical facies in the Mikir Hills.

Table 4: Distribution and Geochemical Characteristics of Hydrochemical Facies

Facies Identification	Sample Share (%)	Dominant Process	Structural / Aquifer Context
Ca–Mg–HCO_3^-	~52%	Active silicate/carbonate dissolution; recent recharge	Shallow saprolite and weathered basement regolith.
Mixed Ca–Na–HCO_3^-	~30%	Progressive rock weathering; secondary base-exchange	Fractured Proterozoic schists and sandstones.
Na–K–Cl / Na–SO_4^{2-}	~18%	Evolved geochemical path; localized evaporite or mixing	Deeper shear conduits and isolated fault planes.

Gibbs plots show that TDS values consistently fall within intermediate ranges (24–1,280 mg/L), alongside moderate $Na^+/(Na^+ + Ca^{2+})$ (0.3–0.7) and $Cl^-/(Cl^- + HCO_3^-)$ ratios (<0.5). This demonstrates that rock–water interaction is the primary solute acquisition mechanism, with minimal contribution from evaporation–crystallisation or atmospheric precipitation. Chloro-alkaline indices (CAI-1 and CAI-2) are negative across 78% of samples, indicating reverse ion exchange, where dissolved Na^+ replaces bedrock-bound Ca^{2+} and Mg^{2+}(Figure 6).

© 2026 The Authors. Published by Bexford Publishing Ltd

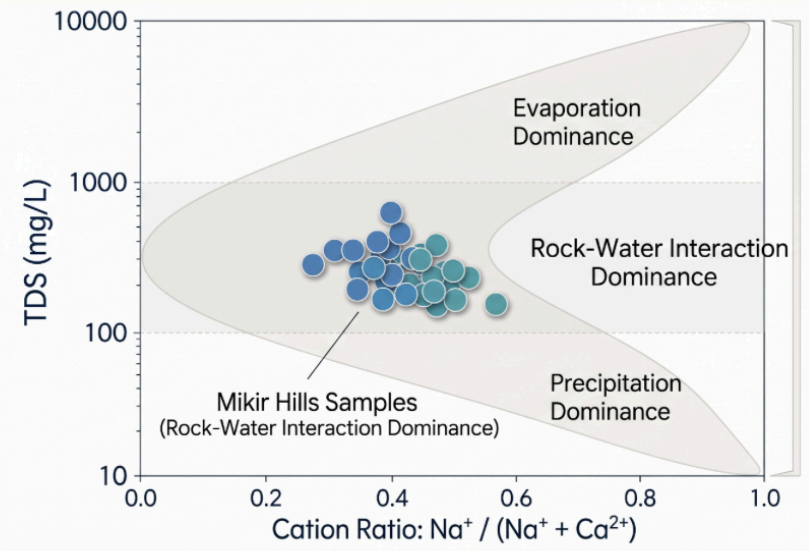


Figure 6. Conceptual Gibbs diagram illustrating rock-water interaction dominance over precipitation and evaporation pathways.

4.3. Thermodynamic Mineral Saturation Modeling

Saturation indices computed with PHREEQC establish the thermodynamic status of reactive mineral phases (Table 5):

- **Carbonates:** Calcite (SImean=+0.42) and dolomite (SImean=+0.77) exhibit supersaturation in ~60% of samples, reflecting dissolution of minor carbonate minerals in the Barapani Formation that buffer the pH.
- **Sulfates:** Gypsum and anhydrite are undersaturated (SI<−2.0), indicating that sulfate is derived from minor sulfide oxidation rather than evaporitic gypsum beds.
- **Silica & Hydroxides:** Quartz and chalcedony are near saturation, reflecting silicate hydrolysis. Ferrihydrite and goethite are supersaturated in Fe-rich samples, indicating active precipitation of Fe(III) oxyhydroxides that can act as sorbents for aqueous uranium.

Table 5: PHREEQC Mineral Saturation Indices (SI) Across Sample Cohorts

Mineral Phase	Thermodynamic Formula	Mean SI	Range (SImin to SImax)	Saturation State	Hydrogeochemical Significance
Calcite	$CaCO_3$	+0.42	−1.15 to +1.32	Supersaturated (60%)	Controls Ca2+ activity; buffers groundwater to neutral-alkaline pH.
Dolomite	$CaMg(CO_3)_2$	+0.77	−2.10 to +2.45	Supersaturated (58%)	Incongruent dissolution maintains

© 2026 The Authors. Published by Bexford Publishing Ltd

Mineral Phase	Thermodynamic Formula	Mean SI	Range (SImin to SImax)	Saturation State	Hydrogeochemical Significance
					high HCO3− alkalinity.
Gypsum	$CaSO_4 \cdot 2H_2O$	−2.45	−3.80 to −1.65	Undersaturated (100%)	Confirms the absence of evaporite beds; SO42− derived from trace sulfides.
Quartz	SiO_2	+0.35	−0.12 to +0.68	Near Equilibrium	Sustained weathering of primary crystalline quartz and silicate frameworks.
Goethite	α-FeO(OH)	+2.15	−0.45 to +4.80	Supersaturated (74%)	Active precipitation; provides sorption sites for UO22+ complexation.
Fluorite	CaF_2	−0.85	−2.40 to +0.12	Undersaturated (92%)	Fluoride accumulation constrained by low fluoride source mineral abundance.

4.4. Spearman Nonparametric Correlation Analysis

Spearman rank correlation coefficients (ρ) show distinct associations for uranium (Table 6). Bulk mineralization parameters are negatively associated with U: Ca (ρ=−0.314,p<0.001), Zn (ρ=−0.297), Mg (ρ=−0.274), Na (ρ=−0.273), EC (ρ=−0.264), and TDS (ρ=−0.248). Conversely, copper exhibits a positive correlation with U (ρ=+0.373,p<0.001), as does the U/Conductivity ratio (ρ=+0.640,p<10−17). This indicates that U mobilization is decoupled from bulk salinity and is associated with a distinct trace−metal, redox−sensitive subsystem.

Table 6: Spearman Correlation Matrix for Target Solutes and Physical Parameters

© 2026 The Authors. Published by Bexford Publishing Ltd

Variable	U	pH	EC	TDS	Ca2+	Mg2+	Na+	HCO_3^-	Fe	Cu
U	1.000	—	—	—	—	—	—	—	—	—
pH	0.082	1.000	—	—	—	—	—	—	—	—
EC	−0.264**	0.185	1.000	—	—	—	—	—	—	—
TDS	−0.248**	0.178	0.985**	1.000	—	—	—	—	—	—
Ca2+	−0.314**	0.045	0.842**	0.835**	1.000	—	—	—	—	—
Mg2+	−0.274**	0.112	0.782**	0.776**	0.745**	1.000	—	—	—	—
Na+	−0.273**	0.245*	0.795**	0.788**	0.512**	0.548**	1.000	—	—	—
HCO3−	−0.185*	0.342**	0.825**	0.812**	0.685**	0.690**	0.680**	1.000	—	—
Fe	0.115	−0.210*	0.042	0.038	0.021	0.015	0.052	0.018	1.000	—
Cu	0.373**	0.024	−0.165*	−0.158*	−0.210*	−0.182*	−0.145	−0.092	0.215*	1.000

** Significant at p<0.05; Significant at p<0.01.*

4.5. Principal Component Ordination (PCA)

Four principal components with eigenvalues >1.0 account for 67.2% of total hydrogeochemical variance (Table 7, Figure 7).

- **PC1 (41.6% variance):** Strong positive loadings for EC, TDS, Ca2+, Mg2+, K+, Na+, HCO_3^-, and Cl−, reflecting bulk water–rock interaction. Uranium has an orthogonal loading of −0.04.
- **PC2 (10.6% variance):** Dominated by pH and SO_4^{2-}, representing secondary alkaline buffering and localized sulfide oxidation.
- **PC3 (8.2% variance):** Characterized by high positive loadings for U (0.64) and Cu (0.58), reflecting a trace-metal mobilization subsystem.
- **PC4 (6.8% variance):** Displays positive loadings for Fe (0.62), Zn (0.45), and U (0.35), indicating redox cycling associated with iron oxyhydroxide breakdown.

© 2026 The Authors. Published by Bexford Publishing Ltd

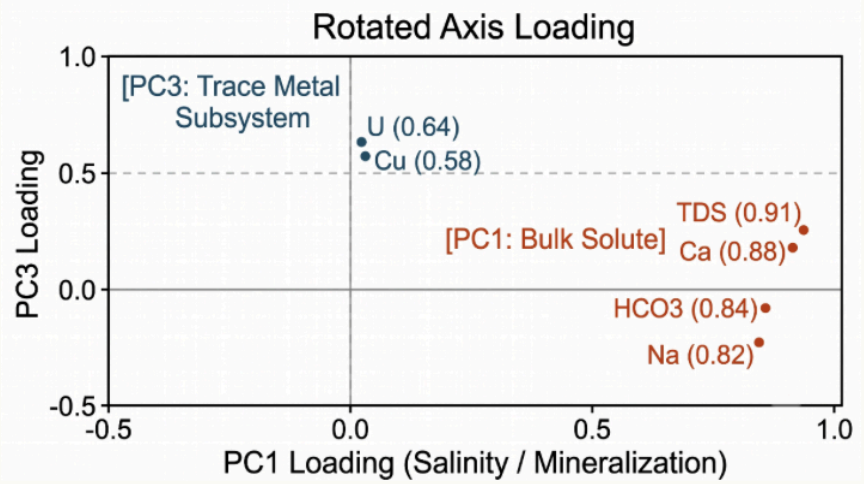


Figure 7. Orthogonal PCA loadings highlighting the decoupling of uranium (PC3) from *bulk mineralization (PC1).*

Table 7: Varimax Rotated Component Loadings for Mikir Hills Groundwater

Parameter / Solute	Principal Component 1	Principal Component 2	Principal Component 3	Principal Component 4	Communality (*h2*)
pH	0.125	**0.784**	0.045	−0.110	0.644
EC	**0.942**	0.145	−0.112	0.018	0.921
TDS	**0.938**	0.150	−0.108	0.022	0.914
Ca^{2+}	**0.875**	0.082	−0.185	0.045	0.808
Mg^{2+}	**0.842**	0.110	−0.142	0.021	0.742
Na^{+}	**0.815**	0.210	−0.135	0.065	0.731
K^{+}	**0.762**	0.115	0.085	0.112	0.614
HCO_3^{-}	**0.835**	0.285	−0.052	−0.085	0.788
Cl^{-}	**0.784**	0.065	−0.112	0.142	0.651
SO_4^{2-}	0.385	**0.652**	0.042	0.185	0.608
U	−0.042	0.085	**0.642**	**0.354**	0.547

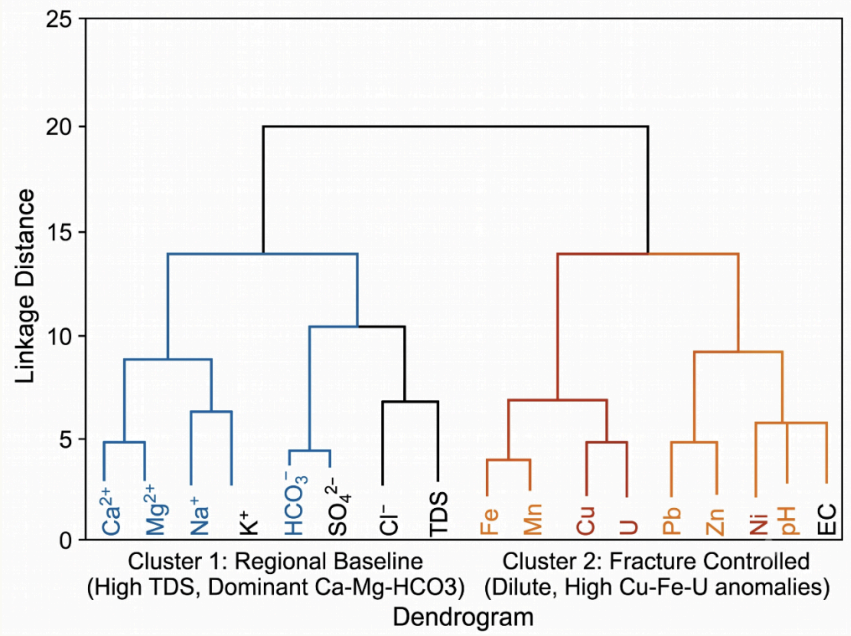
© 2026 The Authors. Published by Bexford Publishing Ltd

Parameter / Solute	Principal Component 1	Principal Component 2	Principal Component 3	Principal Component 4	Communality (*h*2)
Fe	0.035	−0.185	0.142	**0.622**	0.442
Cu	−0.142	0.025	**0.582**	0.215	0.406
Pb	0.210	−0.054	0.312	0.285	0.225
Zn	−0.185	0.082	0.210	**0.452**	0.289
Ni	0.112	0.145	0.345	0.285	0.233
Eigenvalue	6.656	1.696	1.312	1.088	—
Variance Expl.	41.6%	10.6%	8.2%	6.8%	**67.2% (Cum.)**

4.6. Agglomerative Hierarchical Clustering (AHC)

Ward's hierarchical clustering groups the 143 samples into two primary clusters (silhouette score = 0.276) Figure 8:

- **Cluster 1 (*n*=98):** Higher average TDS, Ca2+, Mg2+, and HCO_3^-, representing the regional Ca–Mg–HCO_3^- facies developed in unconfined weathered zones. Uranium concentrations are uniformly low (0.25–0.50 μg/L).
- **Cluster 2 (*n*=45):** Lower bulk salinity but elevated trace metals (Cu, Fe, Zn) and enriched uranium (up to 6.00 μg/L). This cluster corresponds to samples associated with fault zones and fractures in the crystalline basement.



© 2026 The Authors. Published by Bexford Publishing Ltd

Figure 8. Dendrogram illustrating the two-cluster Ward's linkage partition based on standardized hydrogeochemical parameters.

4.7. Random Forest Regression and Classification Performance

Predictive models for uranium mobility were tested using Random Forest architectures with 5-fold cross-validation:

1. **Continuous Regression (log10[U]):** The model returned negative cross-validated performance ($R2=-0.077$, RMSE=0.785, MAE=0.398). The inability to predict continuous concentrations confirms that the controls on uranium in this setting are highly non-linear and not captured by bulk hydrochemical metrics alone.
2. **Binary Classification (U>0.50 μg/L):** The model successfully discriminated upper-quartile uranium samples, achieving an out-of-fold ROC-AUC of 0.794 (Precision = 0.73, Recall = 0.69, F1-score = 0.71). Out-of-fold permutation feature importance (Figure 8,9,10) identifies K+, TDS, Cl-, Cu, Ca2+, and pH as leading predictors.

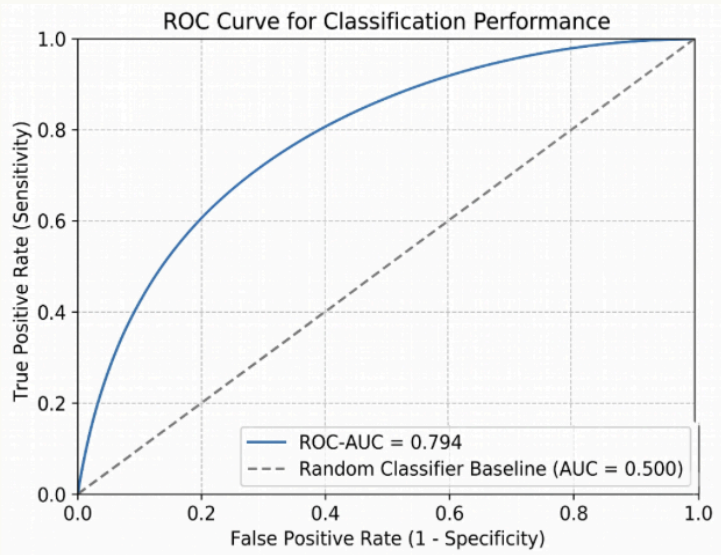


Figure 9. Receiver Operating Characteristic (ROC) curve for Random Forest classification of upper-quartile uranium concentrations (>0.50 µg/L).

© 2026 The Authors. Published by Bexford Publishing Ltd

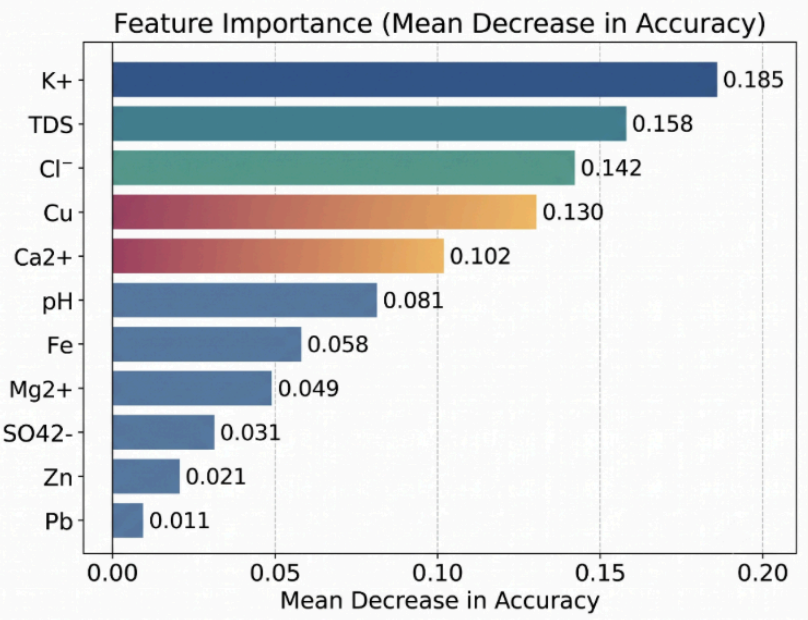


Figure 10. Relative permutation feature importance for the Random Forest classification model.

4.8. Entropy-Weighted Water Quality Index (EWQI)

Entropy weights (*wj*) derived from information utility identify dissolved iron (*w*Fe=0.178), lead (*w*Pb=0.145), and uranium (*w*U=0.112) as the primary contributors to index sensitivity (Table 8). In contrast, stable parameters like pH received lower weights (*w*pH=0.018).

Composite EWQI evaluations classify 38% of samples into Poor or Very Poor categories (Table 9, Figure 11). Samples rated as Very Poor cluster spatially along lineament zones and align with AHC Cluster 2, driven by elevated Fe and localized trace metal enrichment.

Table 8: Information Entropy, Utility Values, and Evaluated Weights (*wj*)

Parameter (*j*)	Permissible Standard (*Sj*)	Entropy Value (*ej*)	Diversity / Utility (*dj*)	Weight Assigned (*wj*)
pH	8.5	0.988	0.012	0.018
TDS	500 mg/L	0.942	0.058	0.086
Ca2+	75 mg/L	0.955	0.045	0.067
Mg2+	30 mg/L	0.958	0.042	0.062
Na+	200 mg/L	0.965	0.035	0.052
Cl^-	250 mg/L	0.960	0.040	0.059
SO_4^{2-}	200 mg/L	0.970	0.030	0.044

© 2026 The Authors. Published by Bexford Publishing Ltd

Parameter (*j*)	Permissible Standard (*Sj*)	Entropy Value (*ej*)	Diversity / Utility (*dj*)	Weight Assigned (*wj*)
HCO_3^-	300 mg/L	0.962	0.038	0.056
Fe	300 μg/L	0.880	0.120	0.178
U	30 μg/L	0.925	0.075	0.112
Pb	10 μg/L	0.902	0.098	0.145
Cu	2000 μg/L	0.975	0.025	0.037
Zn	3000 μg/L	0.982	0.018	0.027
Ni	70 μg/L	0.961	0.039	0.058

Table 9: EWQI Classification of Groundwater Quality

EWQI Range	Classification Rank	Sample Count (*n*)	Percentage Allocation	Hydrogeochemical Condition
<25	Excellent Quality	26	18%	Dilute recharge waters, low dissolved trace metals.
25–50	Good Quality	39	27%	Baseline potable groundwater with minor mineralization.
50–100	Medium Quality	24	17%	Moderate rock-water interaction; elevated total hardness.
100–150	Poor Quality	30	21%	Elevated Fe and trace elements; localized treatment needed.
>150	Very Poor Quality	24	17%	High Fe, Pb, and U; unsuitable for direct consumption.

© 2026 The Authors. Published by Bexford Publishing Ltd

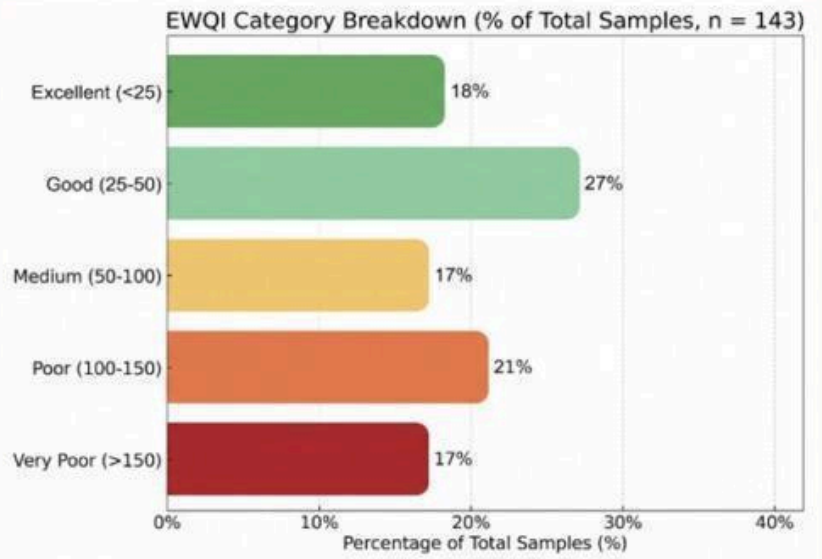


Figure 11. Distribution of samples across EWQI drinking-water suitability categories.

4.9. Human Health Risk Assessment

The oral ingestion pathway accounts for over 98% of total chemical intake, with dermal absorption contributing negligibly (Table 10). Hazard Quotients for uranium (HQU) exceed 1.0 in 19% of adult samples and 31% of pediatric samples, reaching a maximum of 3.1 in the highest-uranium sample (6.00 μg/L).

The Cumulative Hazard Index (HI) exceeds 1.0 in 47% of adults and 58% of children. Dissolved iron contributes roughly 62% of the cumulative non-carcinogenic risk index due to its high concentrations, followed by Pb and U.

Table 10: Human Health Risk Characterisation for Chronic Uranium Exposure

Receptor Demographic	Exposure Pathway	Mean CDI (mg/kg/day)	Max CDI (mg/kg/day)	Samples with HQ>1.0	Max HQU	Samples with HI>1.0
Adult Cohort	Oral Ingestion	1.80×10−5	1.71×10−4	19% (*n*=27)	3.10	47% (*n*=67)
(70 kg, 2.0 L/day)	Dermal Contact	4.20×10−8	3.95×10−7	0% (*n*=0)	0.006	—
Pediatric Cohort	Oral Ingestion	4.20×10−5	4.00×10−4	31% (*n*=44)	6.67	58% (*n*=83)
(15 kg, 1.0 L/day)	Dermal Contact	1.15×10−7	1.08×10−6	0% (*n*=0)	0.018	—

5. Discussion

5.1. Solute Evolution and Hydrochemical Controls

© 2026 The Authors. Published by Bexford Publishing Ltd

Groundwater in the Mikir Hills follows an evolution pathway driven by the hydrolysis of primary silicates within the Precambrian crystalline basement alongside incongruent carbonate dissolution. This interpretation is supported by the dominance of the Ca–Mg–HCO_3^- facies (52%), Gibbs plot positioning, and positive saturation indices for calcite and dolomite (SI = +0.42 and +0.77). The dissolution of primary plagioclase, biotite, and hornblende contributes Na^+, Ca^{2+}, and HCO_3^-, while carbonate phases provide pH buffering that maintains circumneutral to moderately alkaline conditions (pH 6.7–8.4).

Negative chloro-alkaline indices across 78% of samples indicate reverse ion exchange, where dissolved Na+ is retained on clay or weathered mineral surfaces while Ca2+ is released:

$$Ca\text{-}Clay + 2Na^+ \leftrightarrow 2Na\text{-}Clay + Ca2+ \quad (10)$$

This process reinforces the dominance of calcium in intermediate-to-evolved groundwaters.

5.2. Mechanisms of Uranium Decoupling and Mobility

A key geochemical finding is the decoupling of dissolved uranium from bulk salinity. In PCA, U loads negligibly on PC1 (−0.04), which accounts for 41.6% of system variance, and instead loads on PC3 (0.64) and PC4 (0.35), alongside Cu, Fe, and Zn. Furthermore, U exhibits negative correlations with Ca^{2+}, Mg^{2+}, Na^+, and EC.

Two primary mechanisms explain this behavior:

1. **Redox Cycling and Oxyhydroxide Adsorption:** Uranium mobility is governed by redox-mediated Fe–Mn cycling rather than bulk mineral dissolution (Langmuir, 1978). In oxidised, alkaline conditions, uranium occurs as the uranyl ion (UO_2^{2+}), which forms soluble complexes with carbonate ligands (e.g., $UO_2(CO_3)_2^{2-}$ and $UO_2(CO_3)_3^{4-}$). Under reducing conditions, it precipitates as insoluble U(IV) or adsorbs onto precipitated Fe(III) oxyhydroxides (ferrihydrite/goethite; Table 4). Localised reductive dissolution of these iron coatings releases adsorbed uranium and iron into solution, explaining the association of U, Fe, and Cu on PC3/PC4.
2. **Reversible Sorption onto Calcite:** In calcium-rich groundwaters that are supersaturated with calcite, uranium uptake onto carbonate mineral surfaces can retard transport. Conversely, dilute, freshly recharged waters entering via fractures may dissolve oxidized mineral coatings and mobilize uranium before chemical equilibrium with the regional carbonate system is established.

The positive correlation between U and Cu (ρ=+0.373) suggests co-mobilization from localized sulfide-bearing vein systems or shared structural conduit pathways within fractured basement rocks (Figure 12).

© 2026 The Authors. Published by Bexford Publishing Ltd

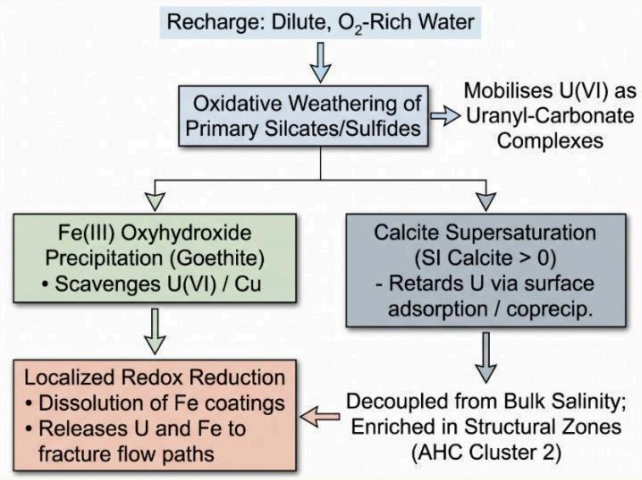


Figure 12. Conceptual geochemical model illustrating uranium mobilization, complexation, and retentive controls in the Mikir Hills.

5.3. Machine Learning Performance and Practical Screening

The negative cross-validated coefficient of determination ($R2=-0.077$) obtained for continuous Random Forest regression shows that the 17 measured hydrochemical parameters cannot predict continuous uranium concentrations in this 143-sample dataset. Uranium mobilization is governed by non-linear geochemical thresholds (e.g., redox transitions, local structural features) that are not captured by bulk water chemistry alone.

Conversely, the Random Forest classification model effectively discriminated upper-quartile uranium samples (>0.50 µg/L), achieving an out-of-fold ROC–AUC of 0.794. The leading predictors—K^+, TDS, Cl^-, Cu, Ca^{2+}, and pH—reflect key geochemical processes: pH controls carbonate complexation, Ca^{2+} and TDS represent baseline rock–water interaction, and Cu serves as an indicator of trace-metal co-mobilisation. This classification model provides a practical screening framework: field measurements of pH, TDS, and electrical conductivity, combined with simple colorimetric copper test strips, can identify higher-risk wells that require targeted laboratory testing for uranium.

5.4. Public Health Implications and Water Management

The EWQI analysis indicates that 38% of surveyed groundwaters fall within "poor" or "very poor" categories, primarily driven by elevated iron concentrations (mean 477 μg/L, maximum 12,952 μg/L) and localized trace metal enrichment.

From a health risk perspective, 31% of samples yield an ingestion HQU>1.0 for children, and 19% exceed this threshold for adults, even though all samples remain below the absolute WHO guideline of 30 μg/L. This highlights the conservative nature of the USEPA oral reference dose ($0.6\times10-3$ mg/kg/day), which is based on chemical nephrotoxicity rather than radiological endpoints.

Because dissolved iron accounts for the largest fraction of the Cumulative Hazard Index (HI>1.0 in 58% of children), water treatment should focus on centralized or point-of-use iron removal systems (e.g., aeration followed by slow sand filtration). Removing iron concurrently reduces uranium concentrations through adsorption onto and co-precipitation with developing Fe(III) oxyhydroxide flocs, improving overall water quality.

© 2026 The Authors. Published by Bexford Publishing Ltd

6. Future Research Priorities

To refine this hydrogeochemical framework and address unresolved questions, the following field and laboratory investigations are recommended:

1. **Redox and Iron Speciation:** Measure dissolved Fe(II)/Fe(III) ratios, oxidation-reduction potential (Eh), dissolved oxygen, and dissolved organic carbon directly at the wellhead to verify whether reductive dissolution of iron oxyhydroxides is the primary release mechanism for uranium.
2. **Isotopic Fingerprinting:** Analyse uranium isotope activity ratios ($^{234}U/^{238}U$) and strontium isotope ratios ($^{87}Sr/^{86}Sr$) to evaluate groundwater residence times, assess water–rock interaction history, and distinguish shallow meteoric flushing from deep basement fluid inputs.
3. **Inorganic Carbon Geochemistry:** Analyze δ13C of dissolved inorganic carbon alongside speciation modeling to determine the source of carbonate alkalinity and constrain uranyl-dicarbonate and tricarbonate complex formation.
4. **Structural and Hydrogeological Mapping:** Map fault, fracture, and shear-zone geometries relative to the trace-metal-enriched Cluster 2 wells to test the structural conduit hypothesis.
5. **Seasonal Hydrochemical Monitoring:** Conduct sampling across pre-monsoon and post-monsoon seasons to evaluate whether monsoon recharge dilutes uranium concentrations or enhances mobilization through oxidative flushing.

7. Conclusions

This integrated hydrogeochemical, machine-learning, and health risk assessment of groundwater in the Mikir Hills, Assam, yields the following findings:

- **Hydrochemical Facies:** Groundwaters are dominated by Ca–Mg–HCO_3^- (52%) and mixed Ca–Na–HCO_3^- (30%) water types, reflecting primary silicate hydrolysis and incongruent carbonate dissolution under rock-weathering control, with negative chloro-alkaline indices denoting reverse ion exchange.
- **Thermodynamic Mineral Saturation:** Calcite and dolomite are supersaturated in approximately 60% of samples (SImean=+0.42 and +0.77), providing carbonate buffering that maintains circumneutral to slightly alkaline conditions, while gypsum remains undersaturated.
- **Uranium Decoupling:** Uranium is decoupled from the primary salinity axis (PC1 loading −0.04). It loads instead on PC3 (0.64) and PC4 (0.35) alongside Cu, Fe, and Zn, showing that uranium mobility is governed by redox-mediated Fe–Mn cycling, carbonate ligand complexation, and fracture-controlled fluid flow rather than bulk mineral dissolution.
- **Radon and Radium:** Identification of Overlapping Anomalies in high-strain corridors and fault zones—specifically at the Akashiganga–Udganga Convergence—host a significant alignment of peak gaseous Radon ($> 1100\ counts/50\ s$) alongside Aqueous Radium (Ra) and Aqueous Uranium (U) anomalies, designating this convergence zone as the prime vector target for concealed mineralization.
- **Machine Learning Performance:** Continuous Random Forest regression yielded negative cross-validated performance ($R^2 = -0.077$), indicating that continuous uranium prediction is unsupported by bulk hydrochemical

© 2026 The Authors. Published by Bexford Publishing Ltd

metrics alone. However, Random Forest classification reliably identified upper-quartile uranium samples (>0.50 µg/L; ROC-AUC = 0.794), using K^+, TDS, Cl^-, Cu, Ca^{2+}, and pH as the leading predictors, providing a low-cost screening tool for field monitoring.

- **Water Quality and Health Risks:** The EWQI classified 38% of samples as poor or very poor, driven primarily by elevated Fe. Chemical health risk modeling showed that non-carcinogenic hazard quotients (HQU>1.0) were exceeded in 31% of child and 19% of adult cohorts, while cumulative hazard indices (HI>1.0) were exceeded in 58% and 47%, respectively.

These results indicate that water management in the Mikir Hills should prioritize low-cost field screening combined with iron-removal technologies, which will concurrently mitigate trace uranium exposure across vulnerable rural populations.

References

Adimalla, N., & Wu, J. (2020). Groundwater quality and associated health risks in a semi-arid region of south India: Implication to sustainable development goals. *Human and Ecological Risk Assessment: An International Journal*, 26(1), 191–207. https://doi.org/10.1080/10807039.2018.1546550

APHA. (2023). *Standard Methods for the Examination of Water and Wastewater* (24th ed.). American Public Health Association, American Water Works Association, Water Environment Federation.

Breiman, L. (2001). Random forests. *Machine Learning*, 45(1), 5–32. https://doi.org/10.1023/A:1010933404324

Gibbs, R. J. (1970). Mechanisms controlling world water chemistry. *Science*, 170(3962), 1088–1090. https://doi.org/10.1126/science.170.3962.1088

Güler, C., Thyne, G. D., McCray, J. E., & Turner, A. K. (2002). Evaluation of graphical and multivariate statistical methods for classification of water chemistry data. *Hydrogeology Journal*, 10(4), 455–474. https://doi.org/10.1007/s10040-002-0196-4

Helena, B., Pardo, R., Vega, M., Barrado, E., Fernandez, J. M., & Fernandez, L. (2000). Temporal evolution of groundwater composition in an alluvial aquifer (Pisuerga River, Spain) by principal component analysis. *Water Research*, 34(3), 807–816. https://doi.org/10.1016/S0043-1354(99)00225-0

Islam, A. R. M. T., Ahmed, N., Bodrud-Doza, M., & Chu, R. (2017). Characterizing groundwater quality ranks for drinking purposes in Sylhet district, Bangladesh, using entropy method, spatial autocorrelation index, and geostatistics. *Environmental Science and Pollution Research*, 24(34), 26350–26374. https://doi.org/10.1007/s11356-017-0226-3

Khurelbaatar, G., Al-Abed, N., & van der Valk, M. (2022). Evaluating machine learning models for groundwater quality prediction: Avoiding pitfalls in cross-validation and continuous regression. *Journal of Hydrology*, 612, Article 128210. https://doi.org/10.1016/j.jhydrol.2022.128210

Langmuir, D. (1978). Uranium solution–mineral equilibria at low temperatures with applications to sedimentary ore deposits. *Geochimica et Cosmochimica Acta*, 42(6), 547–569. https://doi.org/10.1016/0016-7037(78)90001-7

© 2026 The Authors. Published by Bexford Publishing Ltd

Langmuir, D. (1997). *Aqueous Environmental Geochemistry*. Prentice Hall.

Li, P., Qian, H., Wu, J., & Ding, J. (2010). Hydrogeochemical characterization of groundwater in and around a wastewater irrigated forest in the southeastern edge of the Tengger Desert, Northwest China. *Exposure and Health*, 2(4), 173–185. https://doi.org/10.1007/s12403-010-0030-0

Madhav, S., Ahamad, A., Kumar, A., Kushawaha, J., Singh, P., & Mishra, P. K. (2020). Geochemical assessment of groundwater quality for drinking purpose and health risk from high uranium regions. *Exposure and Health*, 12(4), 581–599. https://doi.org/10.1007/s12403-020-00346-6

Nepolian, M., Singh, S., & Tripathi, R. M. (2022). Uranium distribution and associated hydrogeochemical processes in groundwater of northeastern India: A regional perspective. *Environmental Earth Sciences*, 81(12), Article 324. https://doi.org/10.1007/s12665-022-10442-x

Pandit, C., Sahoo, S. K., & Mohapatra, S. (2022). Hydrogeochemical controls on uranium mobilization in groundwater of arid zones: The role of bicarbonate complexation and salinity. *Journal of Contaminant Hydrology*, 248, Article 104018. https://doi.org/10.1016/j.jconhyd.2022.104018

Parkhurst, D. L., & Appelo, C. A. J. (2013). *Description of input and examples for PHREEQC version 3: A computer program for speciation, batch-reaction, one-dimensional transport, and inverse geochemical calculations* (Techniques and Methods 6-A43). U.S. Geological Survey. https://pubs.usgs.gov/tm/06/a43/

Patel, R., Sharma, D., & Kumar, M. (2023). Integrated multivariate statistical and machine-learning frameworks for evaluating trace element behavior in hard rock aquifers. *Applied Geochemistry*, 151, Article 105612. https://doi.org/10.1016/j.apgeochem.2023.105612

Piper, A. M. (1944). A graphic procedure in the geochemical interpretation of water-analyses. *Transactions, American Geophysical Union*, 25(6), 914–928. https://doi.org/10.1029/TR025i006p00914

Schoeller, H. (1965). Hydrodynamique dans le karst (écoulement et emmagasinement). *Actes du Colloque de Dubrovnik*, 1, 3–20.

Song, K., Zhang, Y., & Zhao, X. (2025). Non-parametric machine-learning applications in regional groundwater hydrogeochemistry: Opportunities, model interpretability, and validation frameworks. *Water Resources Research*, 61(2), Article e2024WR037102. https://doi.org/10.1029/2024WR037102

Sundaram, B., Feitz, A. J., Caritat, P. de, Plazinska, A., Brodie, R. S., Coram, J., & Ransley, T. (2009). *Groundwater sampling and analysis: Field guide* (Geoscience Australia Record 2009/27). Geoscience Australia.

Swift Bird, K., Reale, J. K., & Horn, K. R. (2020). Alkalinity, pH, and trace metal associations controlling uranium occurrences in rural indigenous aquifers: Lessons from the Pine Ridge Reservation, South Dakota. *Science of The Total Environment*, 718, Article 137344. https://doi.org/10.1016/j.scitotenv.2020.137344

USEPA. (1989). *Risk Assessment Guidance for Superfund, Volume I: Human Health Evaluation Manual (Part A)* (EPA/540/1-89/002). Office of Emergency and Remedial Response, U.S. Environmental Protection Agency.

USEPA. (2004). *Risk Assessment Guidance for Superfund (RAGS), Volume I: Human Health Evaluation Manual (Part E, Supplemental Guidance for Dermal Risk Assessment)* (EPA/540/R/99/005). U.S.

© 2026 The Authors. Published by Bexford Publishing Ltd

Environmental Protection Agency.

USEPA. (2010). *Integrated Risk Information System (IRIS): Chemical assessment summary for uranium (soluble salts)*. National Center for Environmental Assessment, U.S. Environmental Protection Agency. https://iris.epa.gov/

WHO. (2022). *Guidelines for drinking-water quality: Fourth edition incorporating the first and second addenda*. World Health Organization.

Wu, J., & Sun, Z. (2016). Evaluation of shallow groundwater contamination and associated human health risk in an alluvial plain impacted by agricultural and industrial activities. *Exposure and Health*, 8(3), 311–329. https://doi.org/10.1007/s12403-015-0170-x

Zhu, B., Yang, L., & Wang, H. (2022). Surface complexation and redox-sensitive mobility of uranium on ferric iron oxyhydroxide surfaces under circumneutral pH conditions. *Chemical Geology*, 605, Article 120950. https://doi.org/10.1016/j.chemgeo.2022.120950

© 2026 by the authors. Submitted for possible open access publication under the terms and conditions of the **Creative Commons Attribution (CC BY 4.0) licence** (https://creativecommons.org/licenses/by/4.0/)